JOURNAL OF CATALYSIS 82, 424–441 (1983)

Surface Characterization of Model Urushibara Catalysts

JOSEPH C. KLEIN[1] AND DAVID M. HERCULES[2]

Department of Chemistry, University of Pittsburgh, Pittsburgh, Pennsylvania 15260

Received January 23, 1983; revised March 18, 1983

Surface characterization of model Urushibara catalysts was carried out using ESCA, AES, and SEM. The surface of the Urushibara precursors consists primarily of precipitated nickel covered with a thick oxide coating of Zn or Al, depending on which metal was used to precipitate the nickel from solution. Residual chloride salts of Ni and Zn were also detected on the surface. The precipitated nickel is shown to be sandwiched between the surface oxide layer of Zn or Al and the residual Zn or Al metal used to precipitate the nickel.

INTRODUCTION

Urushibara catalysts were first described in 1952 (*1*). These catalysts can be used for the same catalytic reactions as Raney nickel catalysts. Urushibara catalysts are prepared by a simpler method and are not pyrophoric like Raney catalysts. Conventional Urushibara nickel catalysts are prepared by the addition of $NiCl_2$ to a suspension of Zn dust in water (*1*). A reaction takes place between Ni^{2+} and the Zn metal which precipitates nickel metal presumably on the surface of the zinc. It has been determined that the precipitated nickel does not catalyze hydrogenation reactions. However, after treating the precipitated nickel with concentrated NaOH, catalytic activity comparable to Raney nickel can be achieved (*1*).

A number of variations now exist for the preparation of Urushibara catalysts. To date about 35 different preparations have been reported (*2*). One variation is the substitution of Al for Zn. Also, the leaching process has substituted aqueous KOH, NH_4OH, CH_3CHOOH, or HCl for NaOH. Urushibara catalysts employing metals other than nickel have been prepared by similar precipitation methods. For example, Ni can be replaced by Co, Fe, or Cu. Urushibara catalysts are often designated by first specifying the precipitated metal and then the chemical treatment employed, e.g., U-Ni-B indicates Urushibara nickel activated by treatment with base.

To date Urushibara catalysts have been studied by x-ray diffraction, optical microscopy, electron diffraction, and chemical activity (*2–5*). To date, surface spectroscopy has not been used to characterize these catalysts. We have employed ESCA, AES, and SEM to characterize the surfaces of precipitated nickel using both Al and Zn to precipitate the Ni. We have been able to establish a model for the chemical states of the elements present and their depth distribution in model catalysts. This type of information is important catalytically because it must form the basis for understanding the mechanism of Urushibara catalysts, and for comparing them with their Raney counterparts.

EXPERIMENTAL

ESCA spectra were obtained using a AEI ES200 electron spectrometer with a DS100 data system. An aluminum anode (Al$K\alpha$ 1486.6 eV) was operated at 12 kV and 22 mA. The base pressure was below 2×10^{-8} Torr. The digital data were processed with an HP 2114A computer. Binding energies were measured with a precision of ±0.15

[1] Present address: Texaco Inc., Research Laboratories, P.O. Box 509, Beacon, N.Y. 12508.

[2] To whom all correspondence should be addressed.

0021-9517/83 $3.00

Copyright © 1983 by Academic Press, Inc.
All rights of reproduction in any form reserved.

eV referenced to the C 1*s* line at 284.6 eV. Ion etching was performed using a Physical Electronics 1-keV ion gun operated at a current density of 0.5 $\mu A/cm^2$.

Auger spectra were obtained with a Physical Electronics Model 545 Auger electron spectrometer using a 5-keV primary electron beam. The operating pressure was below 5×10^{-9} Torr. For depth profiles, 5.0×10^{-5} Torr of argon was used with an ion gun operated at 5 keV and an emission current of 30 mA which corresponds to a current density of 1 $\mu A/cm^2$. Peak to peak heights of the Ni LMM, Zn LMM, and Al KLL lines were measured and corrected using published sensitivity factors to calculate the surface concentrations. Scanning Auger micrographs were obtained at a scan width of 340 μm.

Scanning electron micrographs were obtained by the use of a JEOL JSM-50A scanning electron microscope. The electron gun was operated at 25 kV with a beam current of 3×10^{-11} A and a spot diameter of 100 Å. Energy dispersive x-ray analysis was obtained using an Ortec x-ray Li-Si detector.

Precursor materials such as $NiCl_2 \cdot 6H_2O$ (99.9% pure), Zn (99.99% pure) 0.25-mm-thick foil, Al (99.99% pure) 0.25-mm foil, and Zn dust (99% pure) were obtained from Alfa Products of Thiokol.

The modeled Urushibara precipitated nickel was prepared by adding a 1-cm^2 piece of Zn or Al to 50 ml of $NiCl_2$ solution (0.1 g of Ni/ml) at room temperature. The precipitation reactions on Zn were also carried out in boiling water (~100°C). The precipitated nickel was washed with deionized water and dried at 110°C. The nickel chloride solution was prepared by adding 4.04 g of $NiCl_2 \cdot 6H_2O$ to 100 ml of deionized water. The precipitation reaction was allowed to continue until hydrogen evolution stopped (~10 min).

Nickel was also precipitated on zinc dust (U-Ni) to compare the surface characteristics of this model system with the conventionally precipitated nickel system. U-Ni was prepared by adding 10 g of Zn dust to 100 ml of a $NiCl_2$ solution (0.1 g of Ni/ml) at room temperature. The precipitated nickel was washed with deionized water and dried at 110°C.

Cross sections of the model precipitated nickel samples were prepared for SEM analysis by embedding the precipitated Ni on Zn or Al foils in plastic. The embedded samples were then polished on the end to expose the edge of the foils. The samples were coated with a thin film of Au/Pd alloy (60 : 40) to provide a conducting film for the insulating plastic mold.

RESULTS

The Ni $2p_{3/2}$, Zn $2p_{3/2}$, Zn LMM Auger, and Cl $2p$ photoelectron lines were examined to determine the chemical states of Ni, Zn, and Cl on the surface of nickel precipitated on zinc foil (Ni/Zn) and zinc dust (U-Ni). The values of the binding energies and Zn Auger parameters are listed in Table 1. This table also presents binding energy values for Ni $2p_{3/2}$, Al $2p$, and Cl $2p$ photoelectron lines of nickel precipitated on aluminum (Ni/Al). Binding energy values obtained for a few relevant standard compounds are also listed in Table 1.

The Ni $2p_{3/2}$ binding energy for Ni/Zn and U-Ni is 855.6 ± 0.2 eV which corresponds to the Ni $2p_{3/2}$ binding energy of $Ni(OH)_2$. For Ni/Al the Ni $2p_{3/2}$ binding energy (856.4 ± 0.15 eV) is 0.8 eV higher than for Ni/Zn. The Ni $2p_{3/2}$ binding energy of Ni/Al corresponds to $NiCl_2$. Also the Cl $2p$ binding energy of Ni/Al is the same as the Cl $2p$ binding energy of $NiCl_2$. The Zn $2p_{3/2}$ binding energy (1021.7 ± 0.15 eV) and the Auger parameter value (498.3 ± 0.15 eV) for Ni/Zn and U-Ni correspond to the Zn $2p_{3/2}$ binding energy and Auger parameter of ZnO. For Ni/Al the Al $2p$ binding energy (74.5 ± 0.15 eV) is the same as the Al $2p$ binding energy of Al_2O_3.

The relative surface concentrations determined by AES of Ni, Zn, Al, and Cl for Ni/Zn, U-Ni, and Ni/Al are given in Table 2. Published elemental sensitivity factors were used to calculate the relative surface

TABLE 1

Binding Energies of Precipitated Nickel Catalysts

Sample	Binding energies (eV)					
	Ni $2p_{3/2}$	Zn $2p_{3/2}$	Zn Auger LMM	Zn Auger parameter	Al $2p$	Cl $2p$
U-Ni	855.8	1021.7	498.4	523.3		198.8
Ni/Zn dust						
Ni/Zn foil	855.6	1021.7	498.3	523.4		198.7
Ni/Al foil	856.4				74.5	199.0
Zn (metal)		1021.5	494.1	527.4		
ZnO		1021.7	498.2	523.5		
$ZnCl_2$		1021.7	497.0	524.7		198.3
Al (metal)					71.6	
Al_2O_3					74.5	
Ni (metal)	852.3					
NiO	854.0					
$Ni(OH)_2$	855.8					
$NiCl_2$	856.5					199.2

Note. Binding energies were referenced to C 1*s* line at 284.6 eV. Precision is ±0.15 eV.

concentrations (*7*). The surface concentrations listed in Table 2 indicate that both Ni and Cl are not the major elements on the surface of the precipitated nickel. Zn and Al are roughly 8 to 10 times more concentrated on the surface than Ni and Cl for Ni/Zn, U-Ni, and Ni/Al.

Auger element maps of Ni/Zn and Ni/Al are shown in Figs. 1 and 2, respectively. Each Auger map represents a square 340 μm on a side. The bright areas of the Auger element maps indicate regions with the highest surface concentration of an element, while the dark regions correspond to lower surface concentrations. Therefore, the Auger element maps display relative concentration changes over a surface, consistent with the Auger sampling depth (~20 Å).

TABLE 2

Relative Surface Percentage (%) of Precipitated Nickel Determined by AES

Sample	Surface composition (%)			
	Zn	Al	Ni	Cl
Ni/Zn foil	83 ± 1	—	9 ± 2	8 ± 1
Ni/Al foil	—	94 ± 4	4 ± 3	2 ± 0.4
U-Ni				
Ni/Zn dust	75 ± 2	—	7 ± 2	18 ± 1

The Auger element maps of O and Zn for Ni/Zn indicate that regions of high-Zn surface concentration coincide with regions of high oxygen concentration (Fig. 1A and B). The nickel Auger map of Ni/Zn (Fig. 1D) indicates the highest Ni surface concentration is located toward the central section of the map. This same location indicates a low concentration of Cl and a high O concentration. The nickel Auger map also indicates nickel is concentrated in regions near the top central area of the micrograph. In this region the chlorine signal is more intense and the oxygen and Zn signals are lower. The Cl Auger element map also shows an intense Cl signal in a region where concentrated areas of Zn and O are located.

The Auger micrographs of Ni/Al (Fig. 2) indicate direct association between Al and O, because the Al and O mapping images spatially coincide. The Ni and Cl maps also show direct correlation because the intense regions of Ni and Cl correspond to the same locations in the Auger micrographs; they

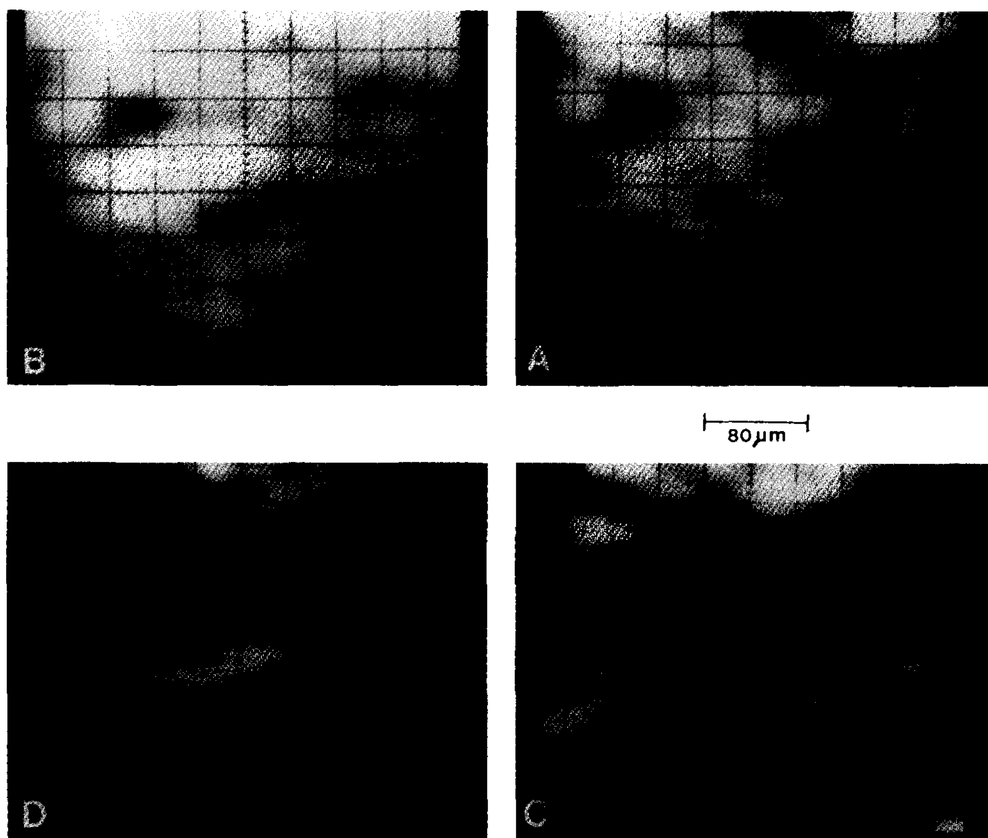

FIG. 1. Auger element maps of Ni/Zn. (A) O KLL, (B) Zn LMM, (C) Cl LMM, (D) Ni LMM.

also correspond to low concentrations of Al and O.

Secondary electron micrographs (SEM) along with energy dispersive X-ray (EDX) element maps of Ni/Zn and Ni/Al are shown in Figs. 3 and 4. In each figure A is the SEM image and B through D are the EDX element maps. The ghost images in the EDX maps are light SEM images of the same sample area superimposed on the EDX map. Superimposing an SEM image on the EDX map was done to orient the EDX maps in relation to the original SEM image. Below we will compare SEM/EDX element maps with those obtained by AES. In doing this comparison it must be remembered that the "surface" sampled by the two techniques differs; for AES the sampling depth is about 20 Å, while for SEM/EDX it is about 1 μm. Therefore, although the term surface is used for each, what it represents differs.

The EDX element images of Ni/Zn (Fig. 3) show that the surface of Ni/Zn is mostly covered with Zn. Ni and Cl do not comprise a large portion of the surface sampled by EDX. The EDX maps of Ni/Zn also indicate that the distribution of Zn, Ni, and Cl is generally uniform across the surface.

The EDX element maps of Ni/Al (Fig. 4) indicate that Ni and Cl are associated on the surface of Ni/Al and in a region distinct from Al. The high concentration areas of Ni and Cl on the right side of the images spacially coincide with the flat irregular shaped regions seen in the SEM image. The areas surrounding the flat objects contain high Al concentrations which is shown in EDX map of Al (Fig. 4B).

ESCA spectra of Ni/Zn and Ni/Al were

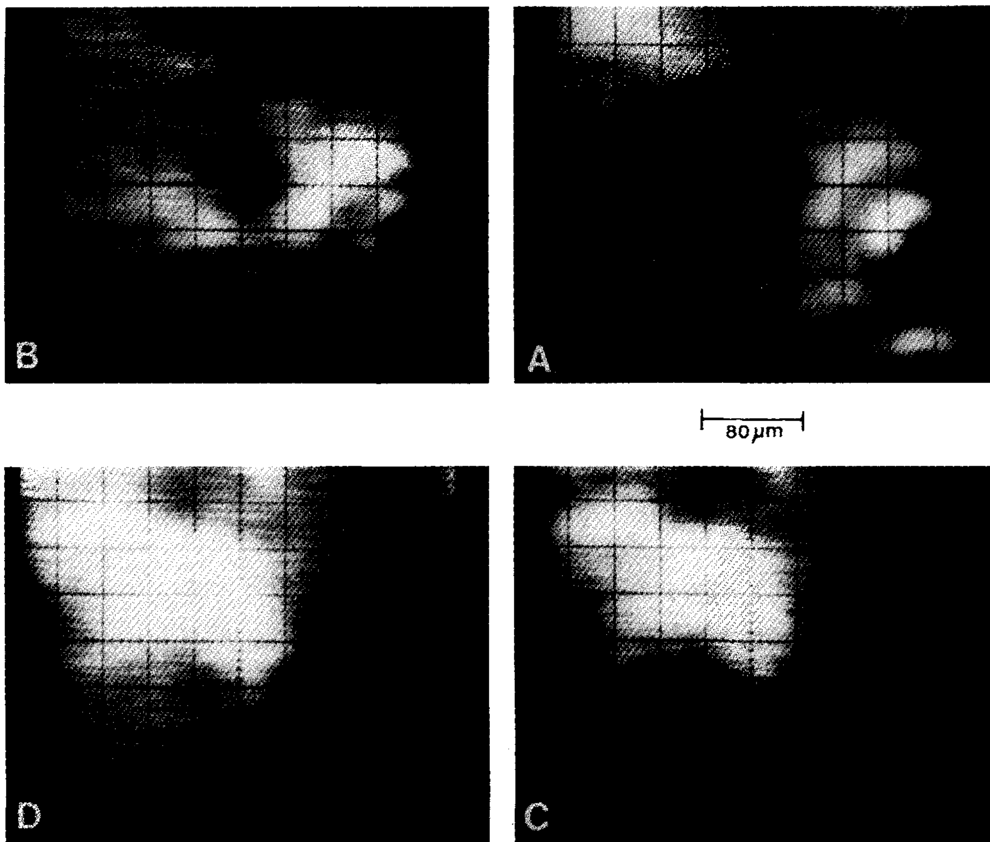

FIG. 2. Auger element maps of Ni/Al. (A) O KLL, (B) Al KLL, (C) Cl LMM, (D) Ni LMM.

obtained at various sputtering times to study Ni/Zn and Ni/Al as a function of depth. Figure 5 shows wide scan ESCA spectra (0–1000 eV) of Ni/Zn and Ni/Al recorded at five different sputtering times (0, 3, 6, 8.5, and 16 h) using a 1-keV Ar ion beam. The Ni $2p_{3/2}$ lines for Ni/Zn and Ni/Al recorded at the same sputtering intervals are shown under higher resolution in Figs. 6 and 7, respectively. Also, the Al $2p$ and Ni $3p$ photoelectron spectra of Ni/Al obtained for the same sputtering experiment are shown in Fig. 8.

The wide scan ESCA spectra (Fig. 5) show an increase in the Ni $2p$ signal intensity as a function of sputtering time for both Ni/Zn and Ni/Al. After 16 h of sputtering the Ni $2p$ lines are the most intense in the ESCA spectra of both systems. Also, the Zn, Al, and Cl signals have almost completely disappeared after 16 h of sputtering for both Ni/Zn and Ni/Al. The Ni $2p_{3/2}$ spectra of Ni/Zn (Fig. 6) show an increase in the metallic nickel signal (852.4 eV) and the disappearance of the higher binding energy signal (855.8 eV) for longer sputtering times. The signal to noise ratio of the Ni $2p_{3/2}$ line increases significantly with longer sputtering times, indicating an increase in Ni surface concentration for longer sputtering time. As will be discussed later these results seem not to be affected by preferential sputtering.

The Ni $2p_{3/2}$ spectra of Ni/Al (Fig. 7) indicate essentially the same results as obtained for Ni/Zn. The higher binding energy Ni $2p_{3/2}$ signal (856.4 eV) corresponding to $NiCl_2$ decreases in intensity and disappears at 16 h of sputtering. The metallic nickel signal (852.4 eV) increases in intensity and

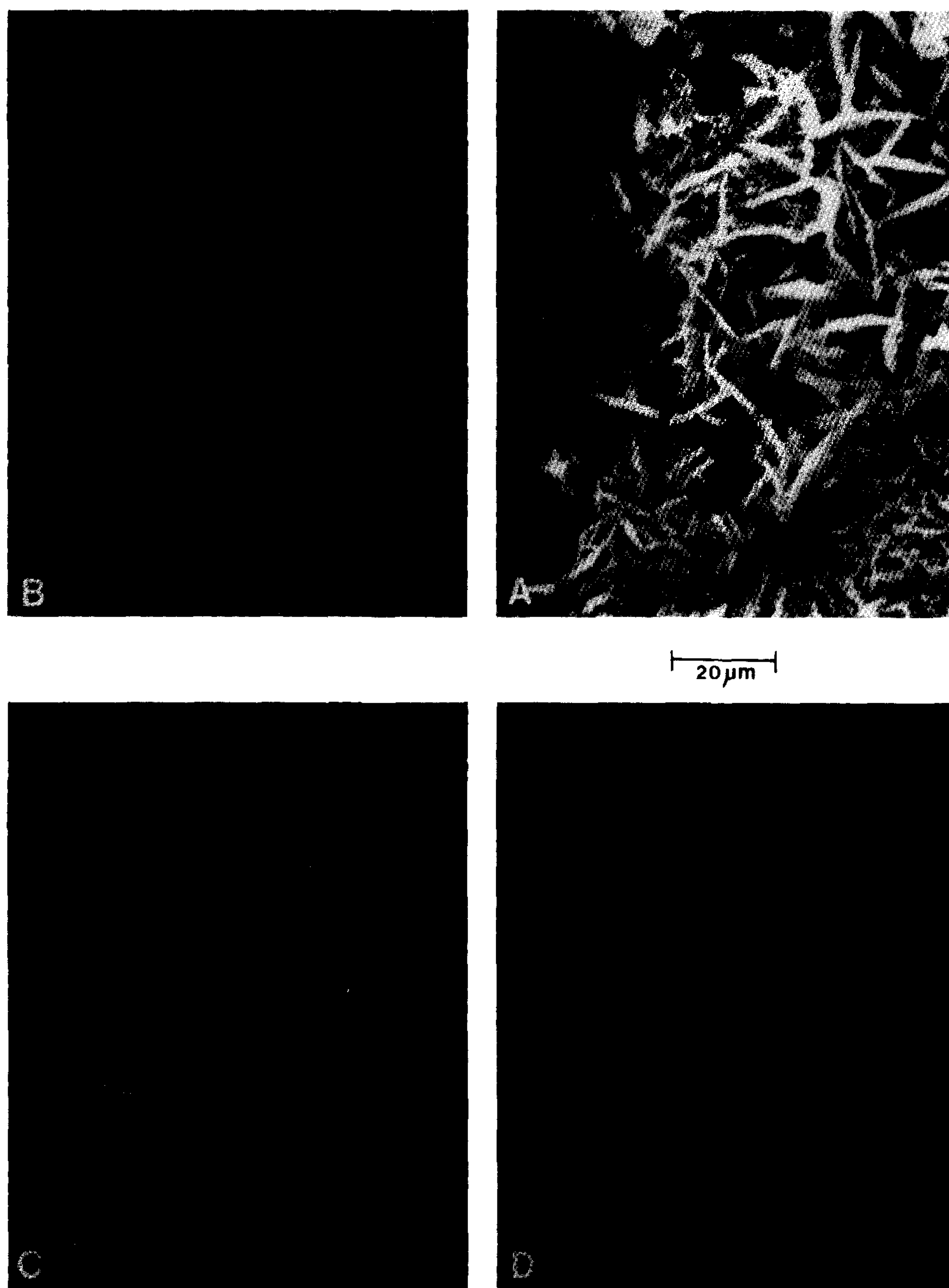

FIG. 3. SEM and EDX images of Ni/Zn. (A) SEM image, (B) Zn EDX map, (C) Ni EDX map, (D) Cl EDX map 1000X.

becomes the only significant signal in the Ni $2p_{3/2}$ spectra after 16 h of sputtering. The increase of the surface nickel concentration with longer sputtering times is not obvious from Fig. 6 because the signal to noise does not increase significantly as it did for Ni/Zn.

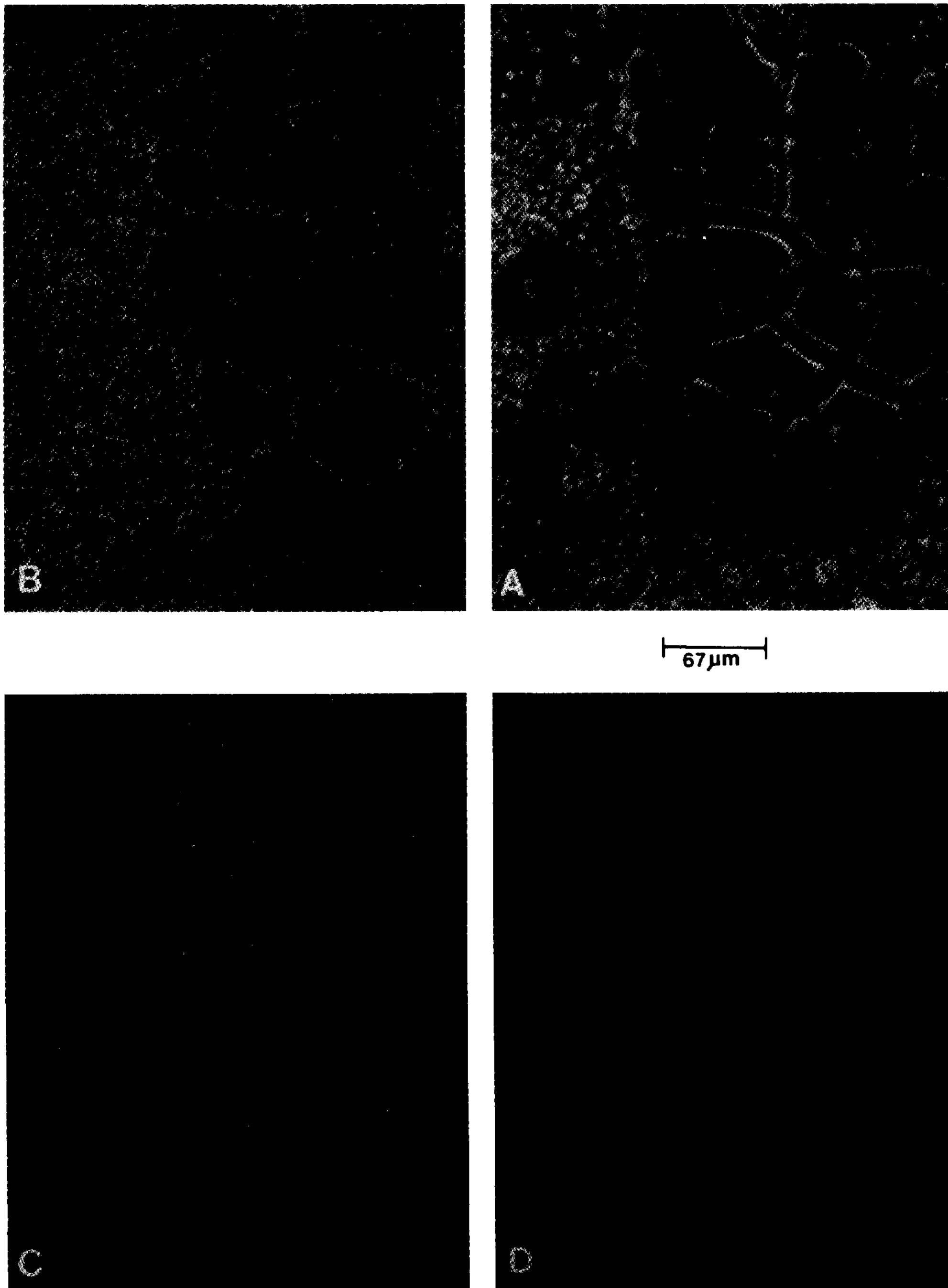

FIG. 4. SEM and EDX images of Ni/Al. (A) SEM images, (B) Al EDX map, (C) Ni EDX map, (D) Cl EDX map 300X.

However, the increase in total nickel signal with longer sputtering times for Ni/Al is seen in Fig. 5.

Figure 8, the Al $2p$ and Ni $3p$ ESCA spectra of Ni/Al, shows the increase in surface nickel at longer sputtering times. The Al $2p$

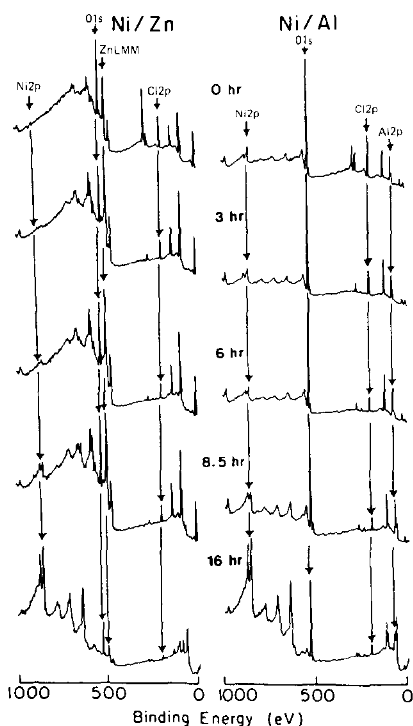

FIG. 5. ESCA spectra of Ni/Zn and Ni/Al as a function of sputtering time. Left hand side, Ni/Zn. Right hand side, Ni/Al.

line in Fig. 8 is located at the high binding energy side of the spectra (74.4 eV). The Al 2*p* signal decreases relative to Ni 3*p* with

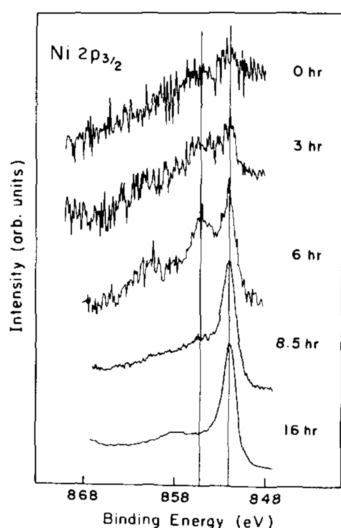

FIG. 6. Ni $2p_{3/2}$ ESCA spectra of Ni/Zn as a function of sputtering time.

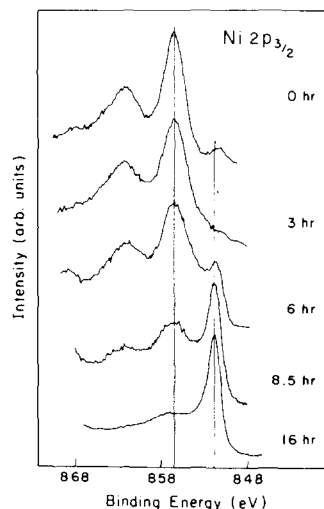

FIG. 7. Ni $2p_{3/2}$ ESCA spectra of Ni/Al as a function of sputtering time.

sputtering. The Ni 3*p* spectrum shifts to lower binding energy and increases significantly in intensity relative to the Al 2*p* signal after 16 h of sputtering.

Auger depth profiles of Ni/Zn and Ni/Al are shown in Figs. 9 and 10, respectively. The Auger depth profiles are plots of peak-to-peak height of given Auger lines as a function of sputtering time. Both Figs. 9A and 10A indicate that the nickel signal increases, goes through a maximum, and then

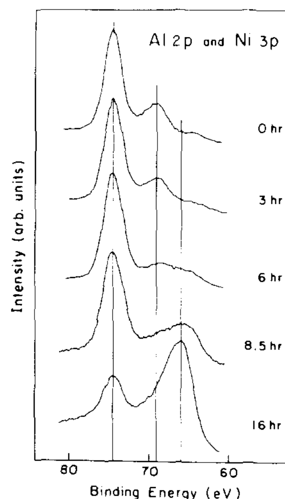

FIG. 8. Al 2*p* and Ni 3*p* ESCA spectra of Ni/Al as a function of sputtering time.

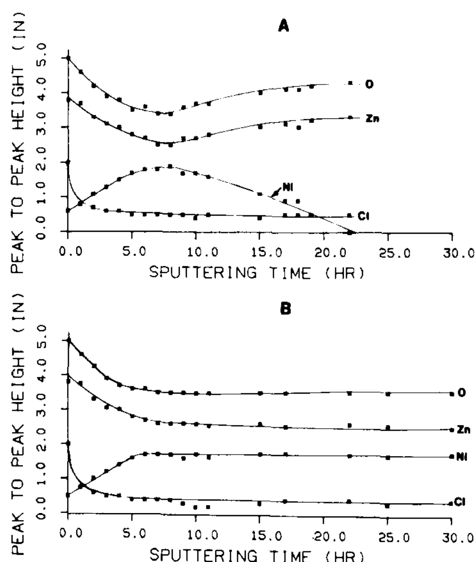

FIG. 9. Auger depth profiles of Ni/Zn. (A) Sputtered through nickel layer. (B) Typical depth profile.

decreases to zero at longer sputtering times. The Zn, O, and Cl signals for Ni/Zn decrease in intensity as a function of sputtering time, going through a minimum when the nickel signal is at its maximum. Figure 9A shows that after 10 h of sputtering the Zn and O signals slowly increase and then level off by 22 h. After 5 h of sputtering the Cl intensity decreases and remains at a low constant value for the rest of the sputtering experiment. The Auger depth profile of Ni/Al (Fig. 10A) also shows a minimum in the Al and O intensities when the Ni intensity is a maximum, at 20 h of sputtering. As the Ni signal decreases after 20 h of sputtering the Al and O signals increase. No Cl was detected in this particular depth profile.

The depth profiles shown in Figs. 9A and 10A for Ni/Zn and Ni/Al, are not typical Auger depth profiles of either system. Most of the depth profiles did not show sputtering through the Ni layer even after 48 h of sputtering. Figures 9B and 10B show typical Auger depth profiles of Ni/Zn and Ni/Al. The depth profile of Ni/Al shown in Fig. 10B contains a Cl depth profile which was not observed in the profile shown in Fig. 10A. Chlorine was removed from the surface within the first 2–3 h of sputtering.

Based on the sputtering rate of Al_2O_3 under our experimental conditions (7 Å/min) which was determined previously (*8*), an estimate was made of the thickness of the Al_2O_3 layer covering Ni/Al. Twenty hours of sputtering is where the Al and O signals reached a minimum and the Ni signal was a maximum which would be the approximate location of the Al_2O_3/Ni interface (*10*). Therefore, for the region depth profiled, the oxide layer is about 0.8- to 0.9-μm thick.

Because most Auger depth profiles did not correspond to sputtering through the Ni layer of either Ni/Zn or Ni/Al, SEM photographs and EDX element maps of Ni/Zn and Ni/Al cross sections were obtained. Figures 11 and 12 are SEM and EDX images of Ni/Zn and Ni/Al cross sections, respectively. The SEM images of cross sectioned Ni/Zn and Ni/Al (Figs. 11A and 12A) indicate four distinct regions. At the top of the SEM image, there is a black zone which is the plastic embedding medium used to hold the cross sectioned samples. Just below the plastic embedding medium is a dark-gray layer. The EDX element maps of Zn and Al indicate that this dark-gray layer consists of Zn and Al for Ni/Zn and Ni/Al,

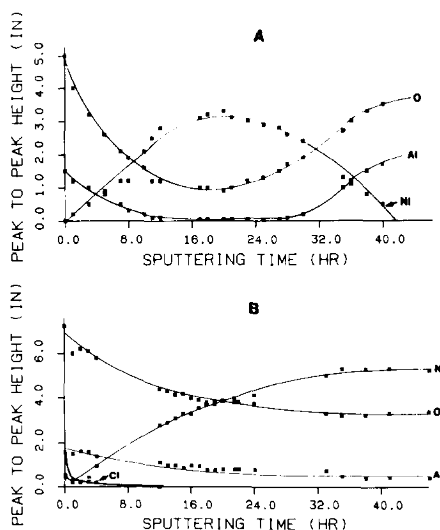

FIG. 10. Auger depth profiles of Ni/Al. (A) Sputtered through nickel layer. (B) Typical depth profile.

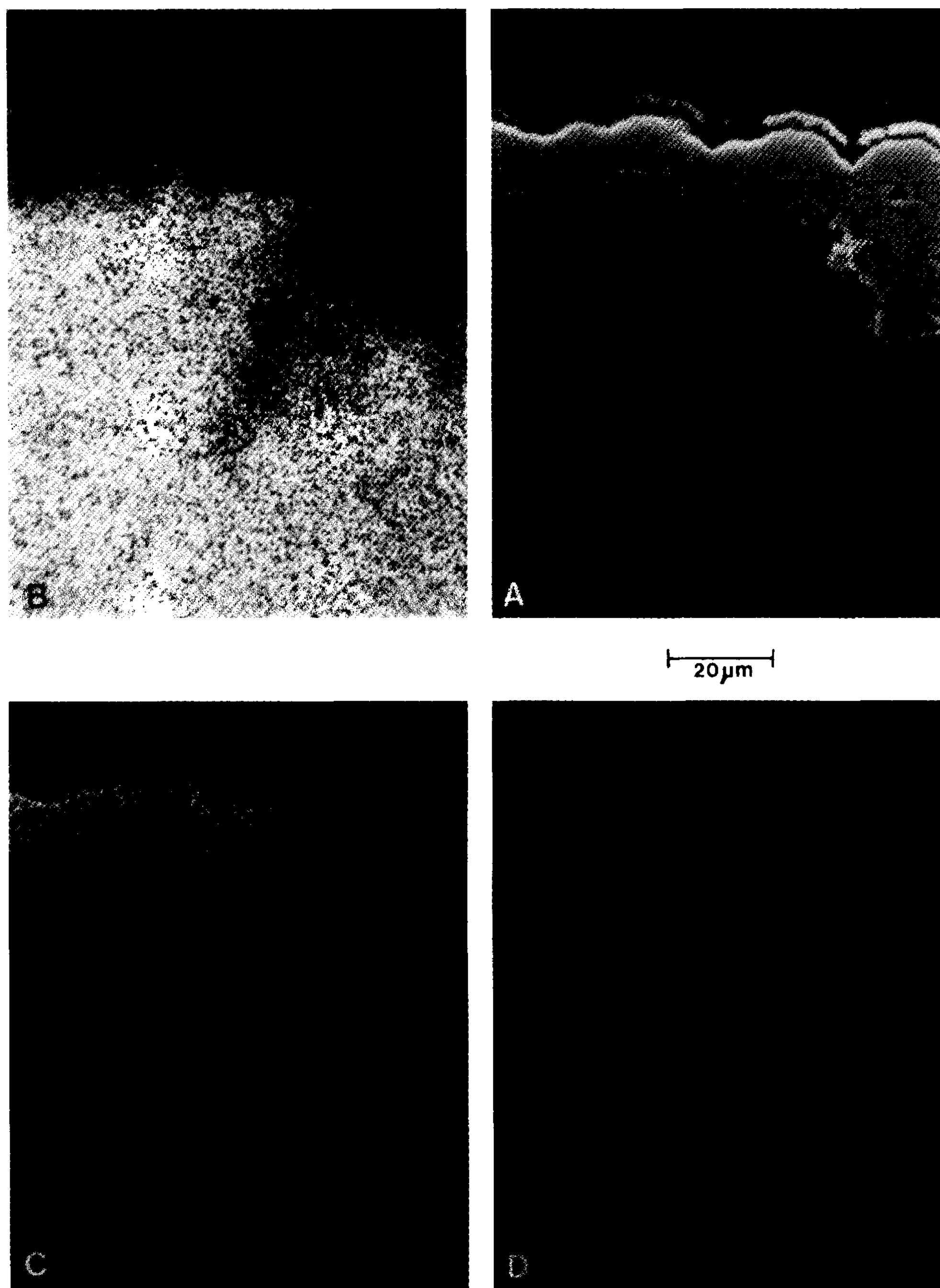

FIG. 11. SEM and EDX images of a cross section of Ni/Zn. (A) SEM image, (B) Zn EDX map, (C) Ni EDX map, (D) Cl EDX map 1000X.

respectively. Below the dark-gray zone there is a light-gray region. The EDX nickel maps show that this region is composed of Ni for both Ni/Zn and Ni/Al. Below the nickel is the fourth region which the EDX maps indicate is composed of Zn and Al for Ni/Zn and Ni/Al, respectively. The Cl EDX maps for both Ni/Zn and Ni/Al indicate no

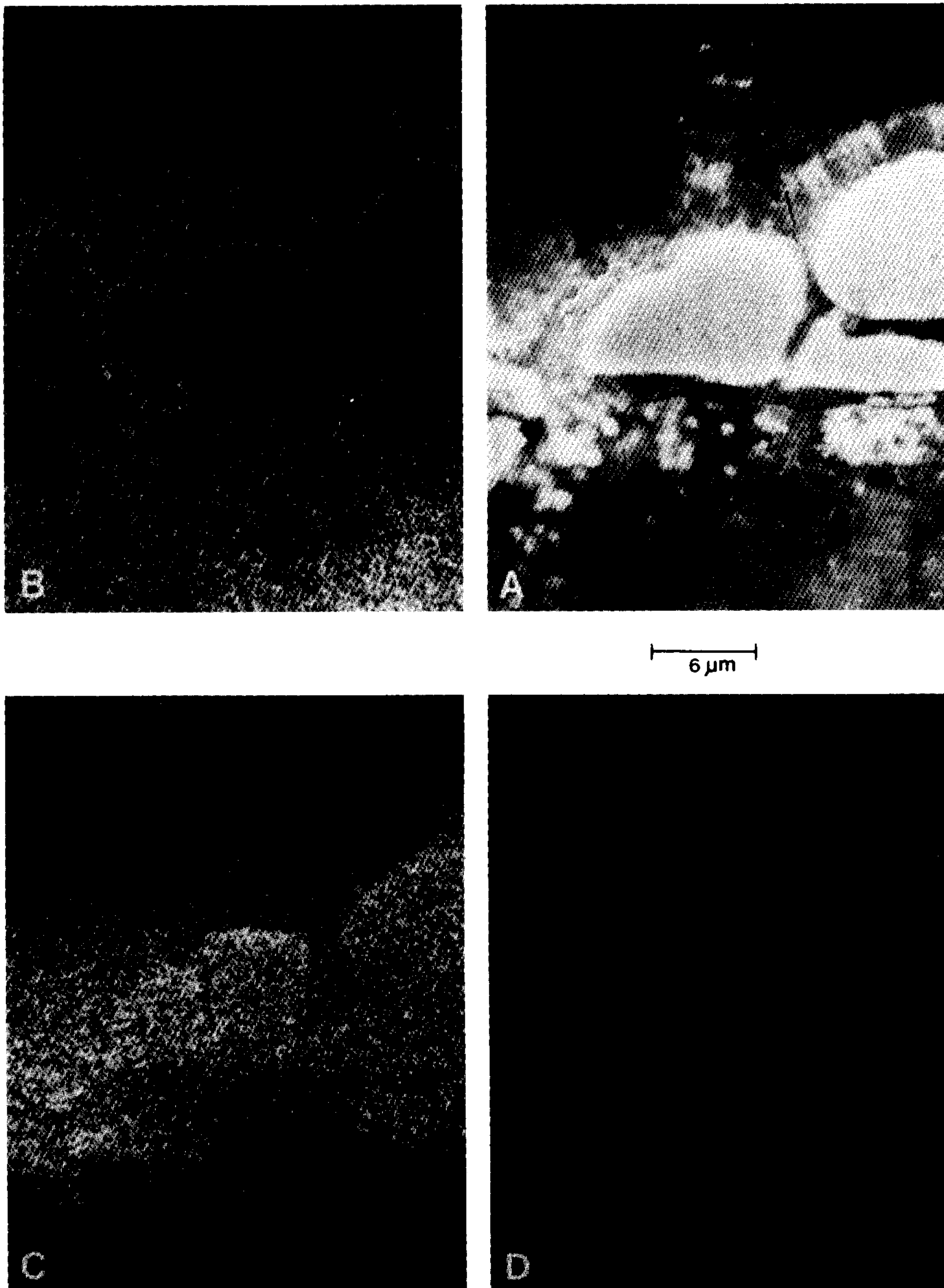

FIG. 12. SEM and EDX images of a cross section of Ni/Al. (A) SEM image, (B) Al EDX map, (C) Ni EDX map, (D) Cl EDX map 3000X.

significant association of Cl with any specific region. Also, the Cl signal per unit area is very small indicating low concentrations of Cl throughout the cross section. The Zn and Al layers which cover the precipitated nickel ranges from 8- to 10-μm thick for both Ni/Zn and Ni/Al. The precipitated nickel layer appears to vary significantly in

thickness, ranging from 10 to 30 μm for both Ni/Zn and Ni/Al.

The thickness of the covering oxide layer determined by some Auger depth profiles is smaller than that determined by SEM. The layers of Ni/Zn and Ni/Al are not uniform in thickness as seen in the SEM cross sections. Therefore, some Auger depth profiles could have been performed at points when the layers are thinner than those shown in the SEM photographs. This latter explanation seems likely to account for the discrepancy between the Auger depth profiles and SEM results, although the alternative of sample rearrangement due to long sputtering times cannot be ruled out.

Ni/Zn was also prepared from a $NiCl_2$ solution at 100°C to observe the effects of high-temperature preparation. The Ni $2p_{3/2}$/Zn $2p_{3/2}$ ESCA intensity ratio for Ni/Zn precipitated at room temperature is 0.10 ± 0.02. For Ni/Zn prepared at 100°C, the Ni $2p_{3/2}$/Zn $2p_{3/2}$ intensity ratio is 0.20 ± 0.06. Precipitating Ni on Zn at 100°C shows an increase in the Ni-to-Zn intensity ratio indicating that there is an increased amount of nickel on the surface for Ni precipitated at 100°C. Figure 13 shows SEM and EDX images of Ni/Zn prepared at 100°C. The EDX analysis of Zn and Cl shows that the surface of Ni/Zn prepared at 100°C has a lower concentration of Zn and Cl. The Ni EDX map on the other hand indicates the surface of the high-temperature precipitation is nickel rich by the high Ni signal density covering the entire surface. The SEM and EDX images of the cross-sectioned Ni/Zn prepared at 100°C (Fig. 14) indicate no significant layer of zinc covering the nickel. The EDX map of Zn (Fig. 14B) does not show a zinc layer between the embedding media and the nickel metal. The Cl EDX map also indicates that Cl is not a major component of Ni/Zn prepared at 100°C.

The surface of Ni/Zn prepared at 100°C structurally has a different surface than Ni/Zn prepared at room temperature. Comparing the SEM image of Ni/Zn prepared at 100°C (Fig. 13) and the SEM image of Ni/Zn prepared at room temperature (Fig. 11), shows that room-temperature preparation creates a less-uniform surface of larger crystals, approximately 10- to 20-μm long. The high-magnification SEM image of Ni/Zn prepared at high temperature (Fig. 15) shows that the high-temperature preparation creates a uniform surface of fine needle-like crystals about 1- to 2-μm long.

DISCUSSION

Comparing the ESCA binding energies and Auger parameters with the AES surface concentrations for Ni/Zn and U-Ni shows that the surface of the modeled nickel precipitated on zinc (Ni/Zn) is similar to the surface of nickel precipitated on zinc dust (U-Ni). The ESCA binding energies of Ni $2p_{3/2}$, Cl $2p$, Zn $2p_{3/2}$, and the Zn Auger parameters listed in Table 1 are the same for both Ni/Zn and U-Ni within experimental error. Therefore, the chemical states of the surface species of both the modeled Ni/Zn and U-Ni can be considered to be the same. The surface concentrations (Table 2) of the modeled and normal Urushibara precipitated nickel catalysts are similar but not identical. In both cases, Zn is the dominant species on the surface. The surface concentration of nickel is essentially the same for both systems. Chlorine appears to be more concentrated on U-Ni than on the modeled system. The increase of surface chlorine on U-Ni is attributed to the greater retention of the Cl after water washing caused by the higher surface area of the powdered zinc. In general, the surface results of the modeled Ni/Zn and U-Ni indicate the model system is a reasonable representation of the actual precipitated nickel Urushibara precursor.

The surface concentrations determined by AES, ESCA, AES depth profiles, and SEM/EDX show that surfaces of Ni/Zn and Ni/Al are covered with Zn and Al, respectively. The Zn Auger parameter for Ni/Zn indicates the presence of ZnO. However, small amounts of $ZnCl_2$ could exist on the surface because the Auger micrographs of

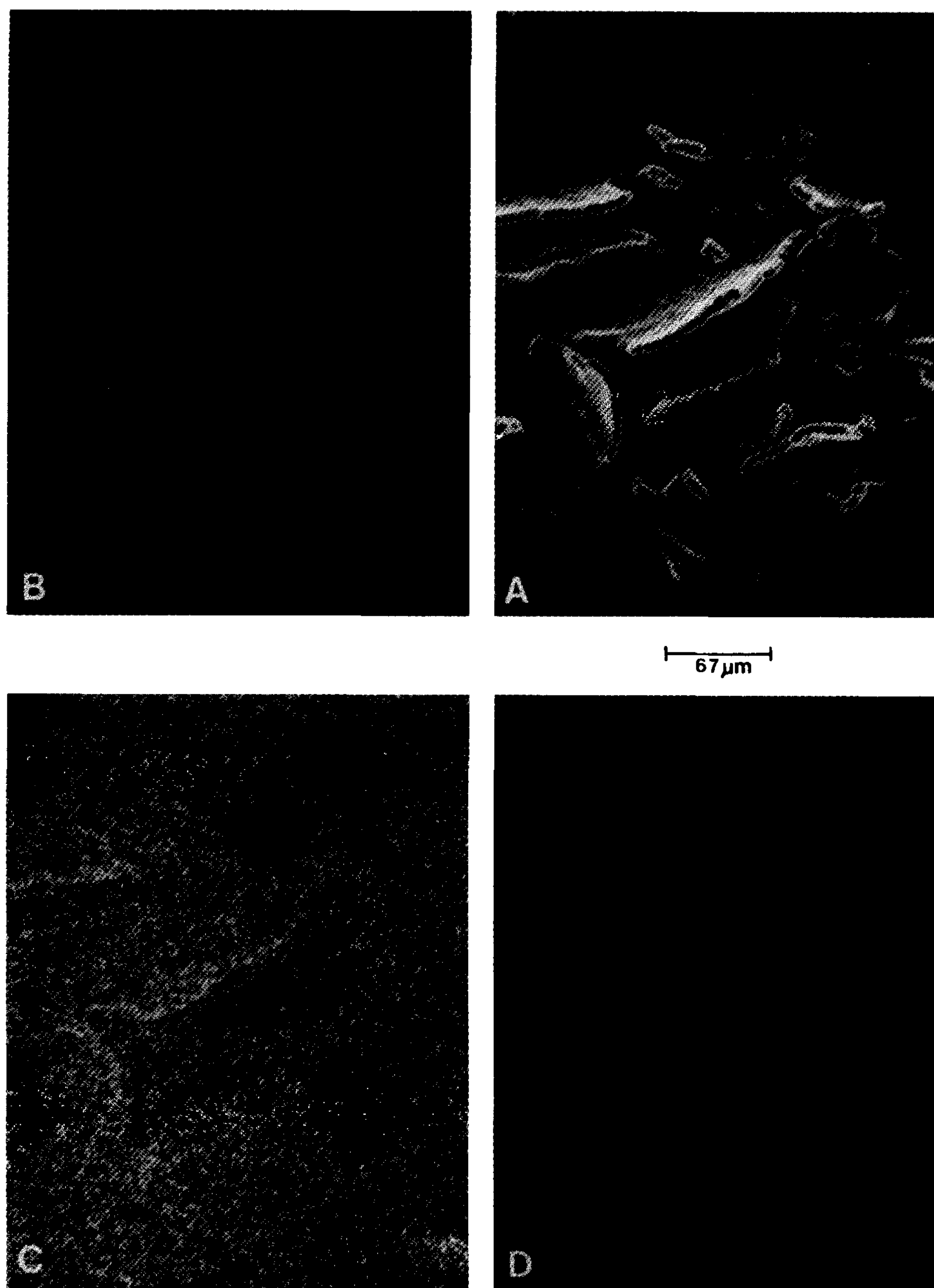

FIG. 13. SEM and EDX images of Ni/Zn prepared at 100°C. (A) SEM image, (B) Zn EDX map, (C) Ni EDX map, (D) Cl EDX map 300X.

Ni/Zn indicate some areas having higher surface concentrations of Zn and Cl in the same region. Both the Al 2*p* binding energies and the Auger micrographs of Ni/Al show only the presence of Al_2O_3 on the surface of Ni/Al.

The nickel species detected on the surface of Ni/Zn appear to be primarily

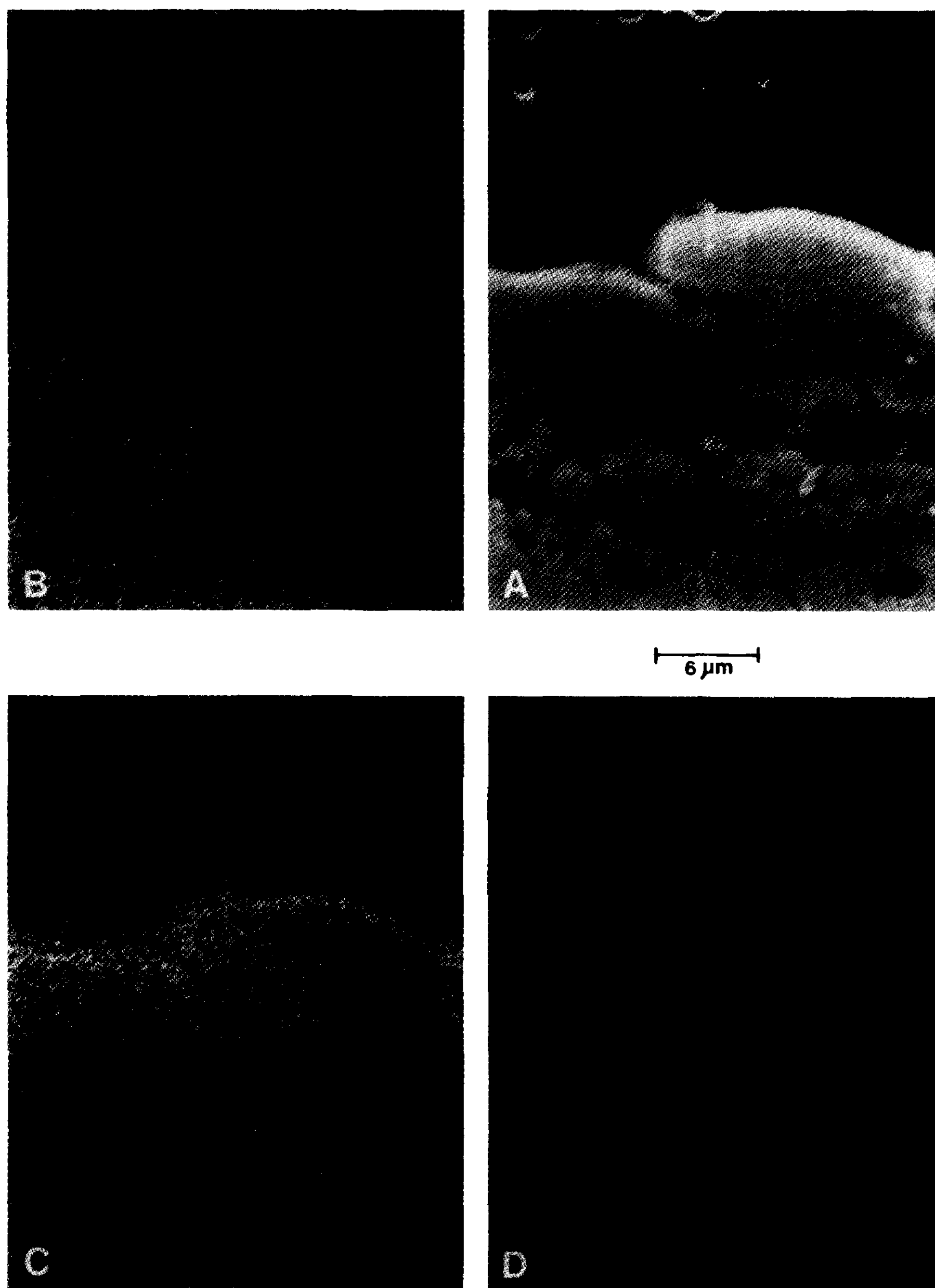

FIG. 14. SEM and EDX images of a cross section of Ni/Zn prepared at 100°C. (A) SEM image, (B) Zn EDX map, (C) Ni EDX map, (D) Cl EDX map 3000X.

$Ni(OH)_2$ and possibly small amounts of $NiCl_2$. The binding energies of the Ni $2p_{3/2}$ spectra for Ni/Zn in Table 1 correlate with the presence of $Ni(OH)_2$. However, the Auger micrographs of Ni and Cl (Fig. 1) indicate areas where relatively high concentrations of Ni and Cl coexist. Therefore, $NiCl_2$ could be present.

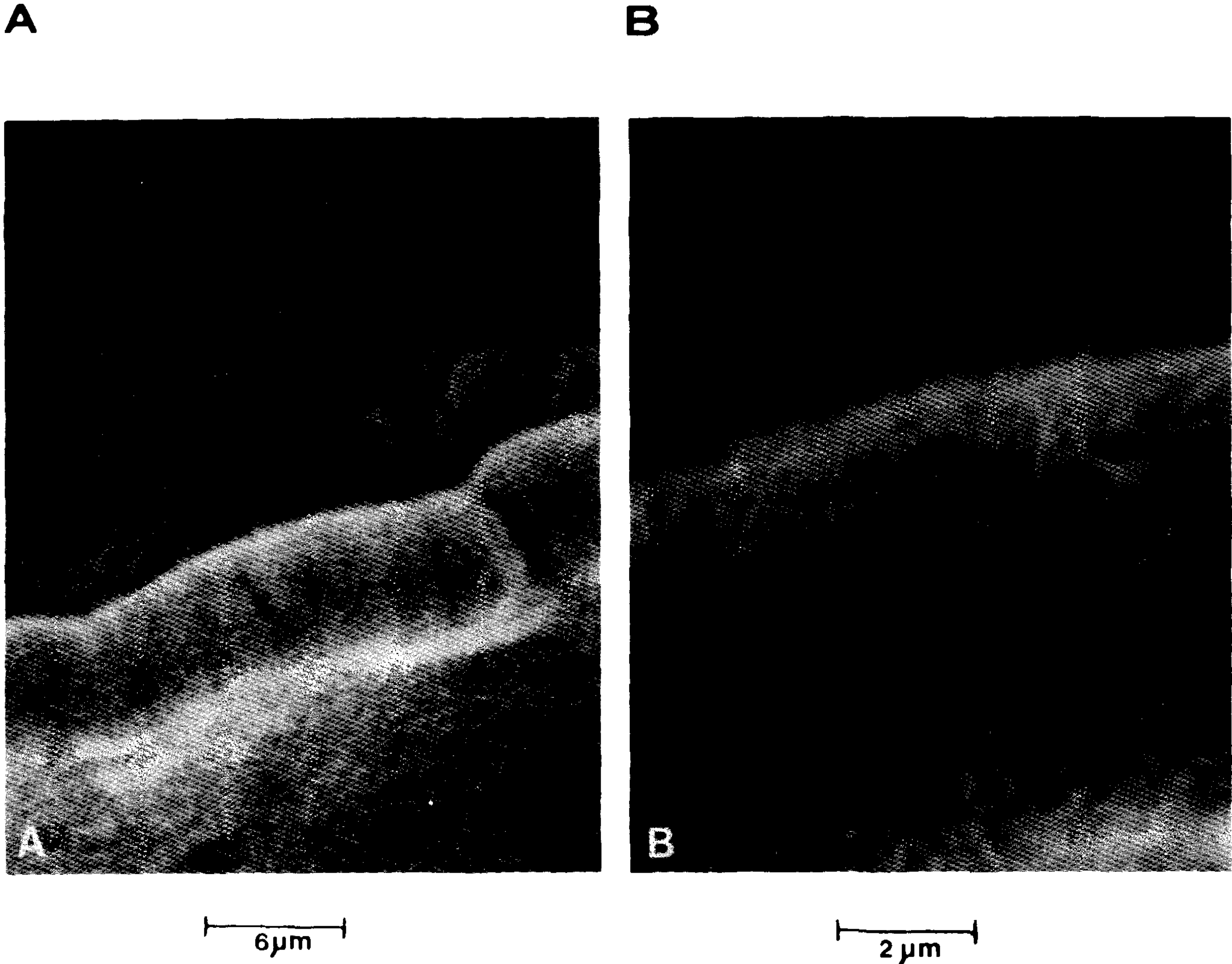

FIG. 15. SEM images of Ni/Zn prepared at 100°C. (A) 3000X. (B) 10,000X.

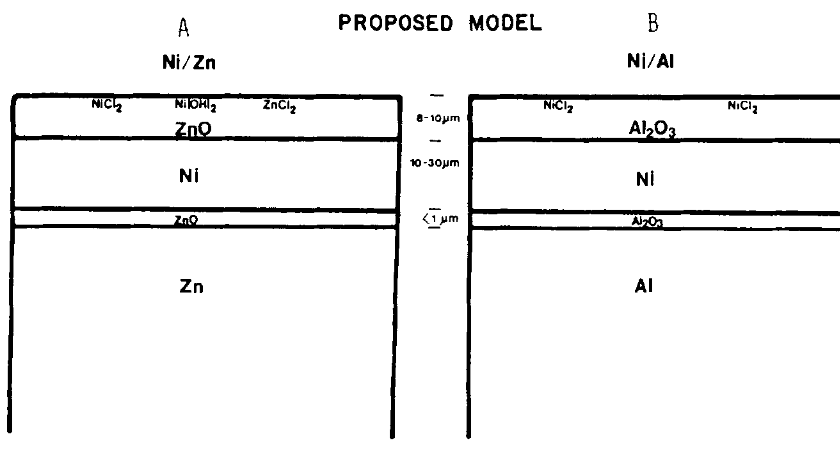

FIG. 16. Proposed model of Urushibara precursor. (A) Ni/Zn. (B) Ni/Al.

The Ni $2p_{3/2}$ binding energy and the Ni and Cl Auger micrographs of Ni/Al indicate that surface nickel is present only as $NiCl_2$. Also, the SEM and EDX images of Ni/Al (Fig. 4) show the presence of $NiCl_2$ because the EDX maps of Cl and Ni spatially coincide only with each other.

The chlorine results determined by AES and SEM/EDX show some discrepancy. The surface concentrations determined by AES (Table 2) indicate the surface of Ni/Zn and Ni/Al consists of between 2 and 8% chlorine. The EDX analysis barely detects chlorine on Ni/Zn and Ni/Al, except where $NiCl_2$ was detected on Ni/Al. The different results between AES and SEM/EDX analysis can be explained on the basis of sampling depths. AES sampling depth is about 20–30 Å; the sampling depth of SEM/EDX is approximately 1 μm. Hence, SEM/EDX samples at considerably greater depths than AES. Based on the different sampling depths, one can conclude that chlorine is concentrated in the upper few atomic layers. This conclusion is consistent with the Auger depth profiles of Ni/Zn and Ni/Al which showed the major portion of chlorine was sputtered away in the first 2 to 3 h.

The ESCA (Figs. 5–8) and AES (Figs. 9–10) depth profiles and the SEM-EDX images (Figs. 11 and 12) of cross-sectioned Ni/Zn and Ni/Al show that the precipitated nickel resides under the oxide films for both Ni/Zn and Ni/Al. Binding energies of the Ni $2p_{3/2}$ spectra recorded at various sputtering times indicate that nickel metal is the dominant peak in the ESCA spectra after 10–20 h of sputtering on both precipitated nickel systems. The SEM and EDX images of the cross sections located the precipitated nickel between the covering oxide layer of Zn or Al and the Zn or Al metal which was not consumed in the precipitation reaction. This conclusion is easily arrived at because Figs. 11 and 12 show that the Ni EDX detected Ni between the two regions of Zn or Al.

A comment should be directed at the ESCA ion etching results of Ni/Zn and Ni/Al. One could argue that ion etching might cause the Ni^{2+} species ($Ni(OH)_2$ and $NiCl_2$) to reduce to the metal during sputtering. However, Kim and Winograd have already shown for $Ni(OH)_2$ (*10*) and we have observed for $NiCl_2$ that Ar ion bombardment does not cause reduction to the metal under the conditions of our experiment. Therefore, the metallic nickel signal observed after sputtering is not a result of the reduction of $Ni(OH)_2$ or $NiCl_2$ by ion bombardment but exists on the catalyst.

Auger depth profiles of Ni/Zn and Ni/Al (Figs. 9A and 10A) indicate the possible existence of ZnO and Al_2O_3 between the

nickel metal and Zn or Al metal interface. Figures 9A and 10A show that as one sputters through the nickel, both the Zn and O for Ni/Zn and the Al and O for Ni/Al show parallel increases in intensity. The increase of the oxygen signal with the increase in Zn and Al signal indicates an oxide region. This conclusion, however, is suspect because it relies on two nonrepresentative depth profiles requiring extremely long sputtering times. At long sputtering times (10 h and longer), sample damage and rearrangement can take place (*9*). Therefore, confirmation of an oxide layer between the Ni and Zn or Al underlayer requires further investigation.

From the results on the two model systems, a simple model of Ni/Zn and Ni/Al was developed. A graphical description of the model is shown in Fig. 16 for room temperature precipitation. According to the model, the catalyst consists of a layer of precipitated nickel 10- to 30-μm thick, underlying a protective oxide layer 8- to 10-μm thick, with small amounts of residual chloride salts present and the Zn or Al which was not consumed in the reduction of the Ni^{2+} ions. It should be noted that hydroxy chlorides of Ni and Zn could exist on the surface of Ni/Zn, however, the surface results do not definitely confirm this. A small oxide layer is suggested between the precipitated nickel metal and the Zn or Al metal, however, this oxide layer has not been fully confirmed.

The Ni/Zn prepared at 100°C differs from the Ni/Zn prepared at room temperature in two ways. First, ESCA showed a larger Ni $2p_{3/2}$/Zn $2p_{3/2}$ ratio for Ni/Zn prepared at 100°C, indicating that the Zn oxide protective film is thinner. Also, the SEM and EDX images of Ni/Zn prepared at high temperature (Figs. 13 and 14) show no appreciable Zn layer covering the precipitated nickel. Second, the SEM images of the high-temperature preparation (Fig. 15) show that the surface is covered with fine needle-like nickel crystals about 1- to 2-μm long. The SEM image of Ni/Zn prepared at room temperature indicates larger crystals about 10- to 20-μm long which are covered with Zn. Therefore, the preparation temperature affects the thickness of the protective oxide layer and the surface structure of the precipitated nickel. Hata has shown by x-ray diffraction line broadening that precipitated nickel on zinc prepared at 100°C contained smaller nickel crystallites (*6*) which is consistent with our results. Hata has also shown that the catalytic activity increased with higher preparation temperature of the nickel precipitation (*6*). This effect is probably related to smaller Ni particle size and therefore greater effective Ni surface area.

SUMMARY

Model Ni/Zn and Ni/Al Urushibara catalysts have been studied to determine the structure of these catalysts. The surface layers of these catalysts are Al and Zn oxides, with some Ni species present. The major Ni species in Ni/Zn is $Ni(OH)_2$, while $NiCl_2$ is the only species observed for Ni/Al catalysts. ESCA and Auger depth profiles, along with SEM/EDX cross sections, were combined to determine the depth distribution of Urushibara catalysts. For the Ni/Zn catalyst one has an outer layer of ZnO (8- to 10-μm thick), a layer of Ni metal (10- to 30-μm thick), a layer of ZnO and the base Zn metal. Similar layering exists for Ni/Al catalysts, with Al_2O_3 substituting for ZnO.

ACKNOWLEDGMENT

This research was supported by the National Science Foundation under Grant CHE81-08495.

REFERENCES

1. Urushibara, Y., *Bull. Chem. Soc. Jpn* **25,** 280 (1952).
2. Hata, K., *in* "New Hydrogenating Catalysts, Urushibara Catalysts," pp. 61–76. Wiley, New York, 1971.
3. Taira, S., *Bull. Chem. Soc. Jpn* **34,** 1294 (1961).
4. Taira, S., *Bull. Chem. Soc. Jpn* **35,** 844 (1962).

5. Urushibara, Y., Yamaguchi, S., and Kobayashi, M., *Bull. Chem. Soc. Jpn* **29,** 815 (1956).
6. Hata, K., *in* "New Hydrogenating Catalysts, Urushibara Catalysts," pp. 86–102. Wiley, New York, 1971.
7. Davis, L. E., MacDonald, N. C., Palmberg, P. W., Riach, G. E., and Weber, R. E., *in* "Handbook of Auger Electron Spectroscopy," 2nd ed., Chap. 1. Physical Electronics Industries, Inc., Eden Prairie, Minnesota, 1976.
8. Klein, J. C., and Hercules, D. M., *Anal. Chem.* **53,** 754 (1981).
9. Castle, J. E., and Hazell, L. B., *J. Electron Spectrosc. Relat. Phenom.* **12,** 195 (1977).
10. Kim, K. S., and Winograd, N., *Surf. Sci.* **43,** 625 (1974).